ADVANCED HEALTHCARE MATERIALS
www.advhealthmat.de

Composite Superelastic Aerogel Scaffolds Containing Flexible SiO_2 Nanofibers Promote Bone Regeneration

*Mingyue Liu, Muhammad Shafiq, Binbin Sun, Jinglei Wu, Wei Wang, Mohamed EL-Newehy, Hany EL-Hamshary, Yosry Morsi, Onaza Ali, Atta ur Rehman Khan, and Xiumei Mo**

Repairing irregular-shaped bone defects poses enormous challenges. Scaffolds that can fully fit the defect site and simultaneously induce osteogenesis and angiogenesis hold great promise for bone defect healing. This study aimed to produce superelastic organic/inorganic composite aerogel scaffolds by blending silica nanofibers (SiO_2) and poly (lactic acid)/gelatin (PLA/gel) nanofibers; the content of SiO_2 nanofibers is varied from 0–60 wt% (e.g., PLA/gel, PLA/gel/SiO_2-L, PLA/gel/SiO_2-M, and PLA/gel/SiO_2-H for 0%, 20%, 40%, and 60% of SiO_2 nanofibers, respectively) to produce a range of scaffolds. The PLA/gel/SiO_2-M scaffold has excellent elasticity and good mechanical properties. In vitro experiments demonstrate that the silicon ions released from PLA/gel/SiO_2-M scaffolds promote the differentiation of rat bone marrow-derived mesenchymal stem cells into osteoblasts, enhancing alkaline phosphatase activity and bone-related genes expressions. The released silicon ions also promote the proliferation of human umbilical vein endothelial cells and the expression of vascular endothelial growth factors, thereby promoting angiogenesis. The assessment of these scaffolds in a calvarial defect model in rats shows good potential of PLA/gel/SiO_2-M to induce bone regeneration as well as promote osteogenesis and angiogenesis. Overall, these organic/inorganic composite scaffolds have good biological activity, which may have broad applications for tissue engineering.

1. Introduction

As a dynamic load-bearing organ, bone tissues remodel throughout the life cycle displaying a certain degree of self-healing. However, bone defects resulting from pathological fracture, osteoporosis, and bone tumor resection are difficult to be healed spontaneously.[1] Effective surgical bone reconstruction has become an integral component for bone defect treatment in clinical medicine. While autografts are the gold standard treatment regimens for bone repair, many limitations, including a limited number of suitable autografts, donor-site associated infection risks, and the need for an extra surgical procedure hamper this approach.[2] Similarly, allogenic grafts face shortcomings, such as the risk of graft rejection, infection, and chronic pain.[3] As an alternative, ceramics, such as calcium phosphate or hydroxyapatite are being clinically exploited to treat bone defects due to their biocompatibility and biodegradability.[4] However, it is difficult to merely use ceramics for bone defect healing due to a poor control over their structure.[5] Injectable bone cement based on calcium phosphate or hydroxyapatite can be easily injected into the surgical site.[6] However, due to bleeding from the defect site during a surgical procedure, the injected bone cement may be diffused away from the implantation site. Cement that hardens upon an injection generally transfers enormous amount of heat due to the chemical curing process,[7] which may be disadvantageous for surrounding tissues. Besides,

M. Liu, M. Shafiq, B. Sun, J. Wu, W. Wang, X. Mo
Shanghai Engineering Research Center of Nano-Biomaterials and Regenerative Medicine
College of Chemistry
Chemical Engineering and Biotechnology
Donghua University
Shanghai 201620, P. R. China
E-mail: xmm@dhu.edu.cn

M. EL-Newehy, H. EL-Hamshary
Department of Chemistry
College of Science
King Saud University
P.O. Box 2455, Riyadh 11451, Saudi Arabia

Y. Morsi
Faculty of Engineering and Industrial Sciences
Swinburne University of Technology
Boroondara, VIC 3122, Australia

O. Ali
School of Chemistry and Chemical Engineering
Tiangong University
Tianjin 300387, P. R. China

A. ur R. Khan
Department of Biotechnology
The University of Azad Jammu & Kashmir
Muzaffarabad 13100, Pakistan

The ORCID identification number(s) for the author(s) of this article can be found under https://doi.org/10.1002/adhm.202200499

DOI: 10.1002/adhm.202200499

injectable cement exhibits poor interconnectivity,[8] which may hinder host-implant integration and neo-vessel formation[9] as well as pose inflammation and infection. Therefore, the preparation of three dimensional (3D) porous scaffolds that can promote the integration of the host and the implant and can better adapt to the bone defect site has important research significance.

Previously, different types of approaches have been undertaken to afford 3D porous scaffolds for bone tissue engineering (BTE), including salt-leaching[10] and thermally-induced phase separation (TIPS).[11] But scaffolds prepared by salt leaching are brittly displaying poor pore-interconnectivity, those fabricated by TIPS may be too dense with the pore size less than 10 microns, which may not be conducive for cell growth. However, micro/nanofabrication techniques, such as electrospinning[12] and 3D printing afford precision-based and tunable scaffolds.[13] Greiner et al. leveraged electrospun short nanofibers to afford open porous 3D scaffolds.[14] By optimizing the content of short nanofibers and freeze-drying parameters, a 3D scaffold with a pore size of up to 100 microns and a porosity of more than 90% was fabricated, which not only promoted cell growth but also allowed neo-vessel formation, thereby promoting host-implant integration for the constructive remodeling of scaffolds post-implantation. Different kinds of polymers can be used for the production of 3D porous degradable scaffolds, including poly(L-lactide)/gelatin (PLA/gel),[15] poly(L-lactide)/poly(ϵ-caprolactone) (PLA/PCL),[16] poly(caprolactone) (PCL),[17] and PLA/chitosan.[18] However, as the natural bone is an inorganic-organic hybrid, biomimicking the native microenvironment may hold great promise for BTE.[19] Inorganic/organic hybrids offer a promising platform for BTE, which may also promote host integration and neovascularization. Therefore, interrogating osteogenesis/angiogenesis by the release of metallic ions (i.e., silicon ions) while realizing bone microenvironment mimetic mechanical properties holds great promise. In previous studies, an array of nanomaterials, including bioactive glasses has been leveraged to promote bone repair as well as mimic native bone-like microenvironment. Noticeably, silicon ions were shown to play an important role in stimulating cell proliferation as well as promoting osteogenic differentiation and angiogenesis.[20] Besides, silicon is an essential inorganic component in metabolic processes related to connective tissue development and bone metabolism. Silicon ions promote the blood vessel and bone formation by stimulating the interaction between endothelial cells (ECs) and BMSCs.[21]

The development of scaffolds with good mechanical properties is also one of the main challenges for tissue-engineered bone scaffolds. High porosity and an interconnected open porous structure of scaffolds are integral for the transport of nutrients and the diffusion of oxygen during tissue formation.[22] However, these properties must combine structural stability, mechanical strength, and elasticity of 3D scaffolds to better withstand local tissue stress in order to maintain high porosity and open scaffold structure for a long time. Superelastic materials generally refer to shape memory and shape recovery materials. The shape-memory materials can ensure that the scaffolds are implanted in a compressed state and adapt to the bone defect through minimally invasive surgery. Previous studies have shown that 3D scaffolds with shape memory capabilities were superior for transplantation into complex bone defects as well as mechanical adaptability during regeneration. PLA/gel-based nanofiber sponges exhibiting high elasticity, porosity, and good mechanical properties have been shown to promote cartilage regeneration.[15] For BTE, superelastic scaffolds, devoid of inorganic components may not accurately mimic the natural bone microenvironment. While bioceramics and inorganic nanoparticles are commonly used as integral components of bone scaffolds, the poor compatibility between organic and inorganic components compromises elastic properties and promotes biodegradation of these scaffolds.[23] To address these shortcomings, we fabricated superelastic composite nanofibrous aerogel scaffolds by utilizing chemical bonding between flexible short SiO_2 nanofibers and PLA/gel nanofibers.

Herein, we proposed the fabrication of inorganic-organic hybrids aerogel scaffolds by using electrospun short nanofibers which may not only promote osteogenesis and angiogenesis but can also mimic the structural and morphological features of the natural bone ECM. We separately fabricated PLA/gel nanofibers and SiO_2 nanofibers by using electrospinning. Thereafter, we designed open porous 3D scaffolds exhibiting elasticity and shape-memory functions by thermally crosslinking PLA/gel and SiO_2 short nanofibers. We thoroughly characterized physicochemical and biological properties of scaffolds. As a proof-of-concept, we evaluated these scaffolds in a calvarial defect model in rats.

2. Results

2.1. Physiochemical Properties of PLA/gel/SiO_2 Aerogel Scaffolds

To increase the processability, we blended the sol obtained from the hydrolysis of tetraethyl orthosilicate (TEOS) along with an aqueous PVA solution to afford a uniform solution that could be readily electrospun to form flexible nanofibrous membranes. Fourier-transform infrared spectrophotometer (FTIR) spectrum of the PVA/Si nanofibrous membranes showed a characteristic peak at 945 cm^{-1}, corresponding to the C–H stretching vibration, which was not found in the spectrum of inorganic SiO_2 nanofibrous membranes (Figure S1, Supporting Information). This indicates that PVA has been completely removed from the nanofibrous membrane by calcination. The resulting membrane was composed of smooth SiO_2 nanofibers exhibiting good flexibility (Figure S2A, Supporting Information). In comparison with the nanofiber membranes before calcination, the fiber diameter of the SiO_2 nanofiber membranes was relatively small (Figure S2B,C, Supporting Information). The TEM image of a single SiO_2 nanofiber also showed smooth surface morphology without defect (Figure S2D, Supporting Information). The obtained SiO_2 nanofiber membranes were next processed into individual short SiO_2 nanofibers by mechanical pulverization and dispersion in tertiary butanol (tert-butanol). Similarly, individual PLA/gel short nanofibers were prepared as described in our previous report.[15] Thereafter, SiO_2 and PLA/gel short nanofibers were fabricated into PLA/gel/SiO_2 aerogel scaffolds. These aerogel scaffolds prepared by using the same sized molds were of bright white color, which turned to pale yellow color after thermally-induced crosslinking. While the PLA/gel aerogel scaffolds shrank after crosslinking, the scaffolds containing SiO_2 nanofibers remained unaffected. Once hydrated with PBS, the PLA/gel aerogel scaffolds deformed due to their poor mechanical properties. Contrarily, the PLA/gel/SiO_2 aerogel scaffolds remained morphologically unchanged due to their reinforcement with the SiO_2

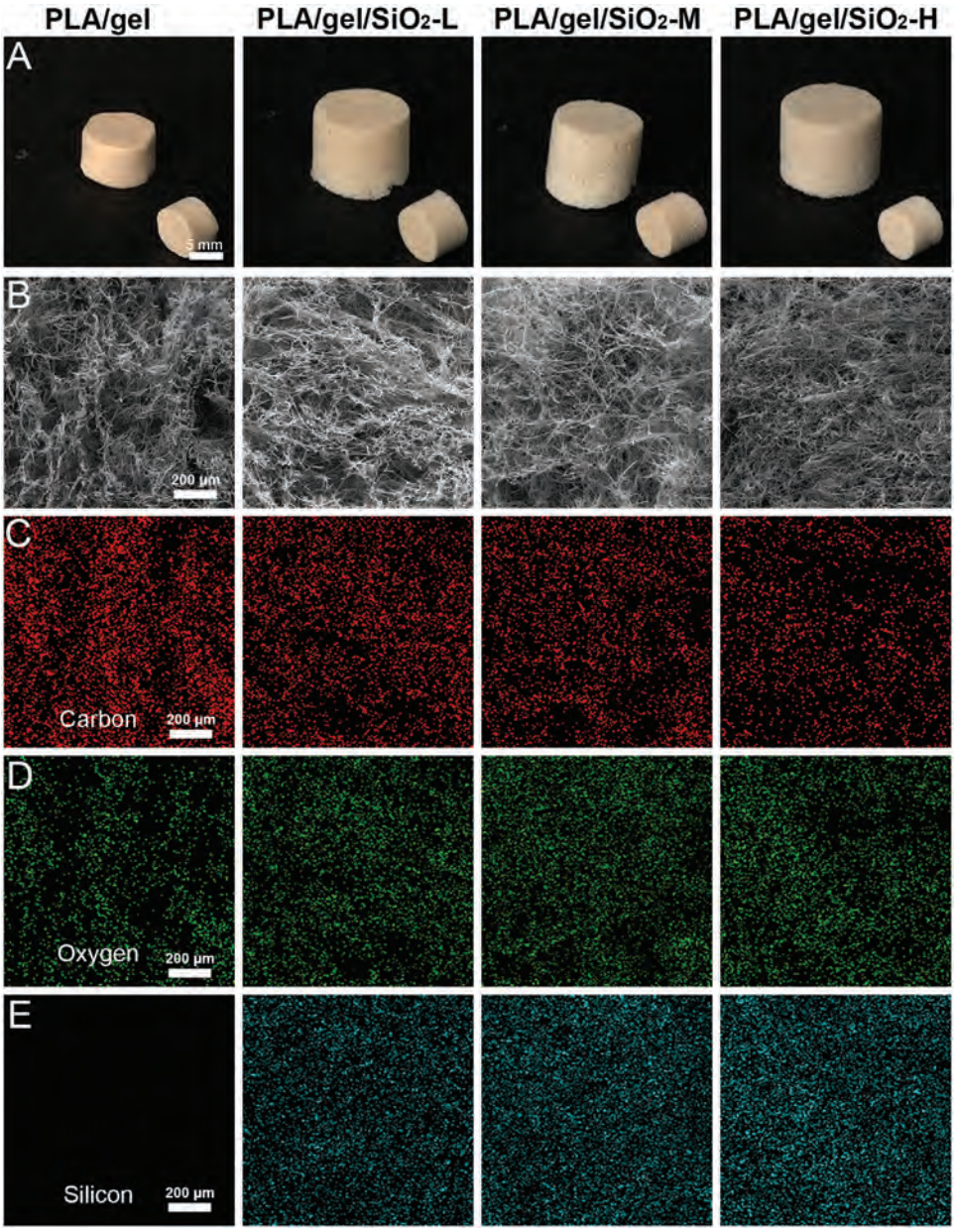

Figure 1. Morphology and characterization of aerogel scaffolds. A) Photographs and B) SEM images of 3D porous composite nanofiber aerogel scaffolds with different content of SiO_2 nanofibers. Elemental mapping images of C) Calcium, D) Oxygen, and E) Silicon of various aerogel scaffolds. Scale bars = A) 5 mm and B–E) 200 µm.

nanofibers (Figure S3, Supporting Information). The PLA/gel aerogel showed a smooth surface with a greatly shrunken size after thermal crosslinking. In contrast, PLA/gel/SiO_2 aerogel scaffolds exhibited porous surface morphology without an evident volume change (**Figure 1**A). Morphologically, PLA/gel aerogel scaffolds exhibited compact nanofiber sheets along with mesopores (Figure 1B). On the other hand, PLA/gel/SiO_2 aerogels showed loose fibers morphology and reduced fiber binding displaying uniform pores with an increase in the SiO_2 nanofiber content. EDS mapping confirmed homogeneous elemental distribution of carbon (Figure 1C), oxygen (Figure 1D), and silicon (Figure 1E), implying that SiO_2 nanofibers were evenly distributed within these PLA/gel/SiO_2 aerogel scaffolds. At the same time, the mass ratio of the silicon elements of different scaffolds can be obtained by EDS semi-quantitative analysis, which revealed a concomitant increase in the silicon content with an increase in the proportion of SiO_2 nanofibers in the scaffolds (Figure S4, Supporting Information).

FTIR spectrum of SiO_2 nanofibers manifested characteristic peaks at 802 and 1051 cm^{-1}, corresponding to the Si–O (Si–O–Si) stretching vibration[24] (**Figure 2**A). While these peaks were not observed in the spectrum of PLA/gel aerogel scaffolds, PLA/gel/SiO_2 aerogel scaffolds exhibited these peaks. The characteristic peaks of amide I and amide II were observed at 1633

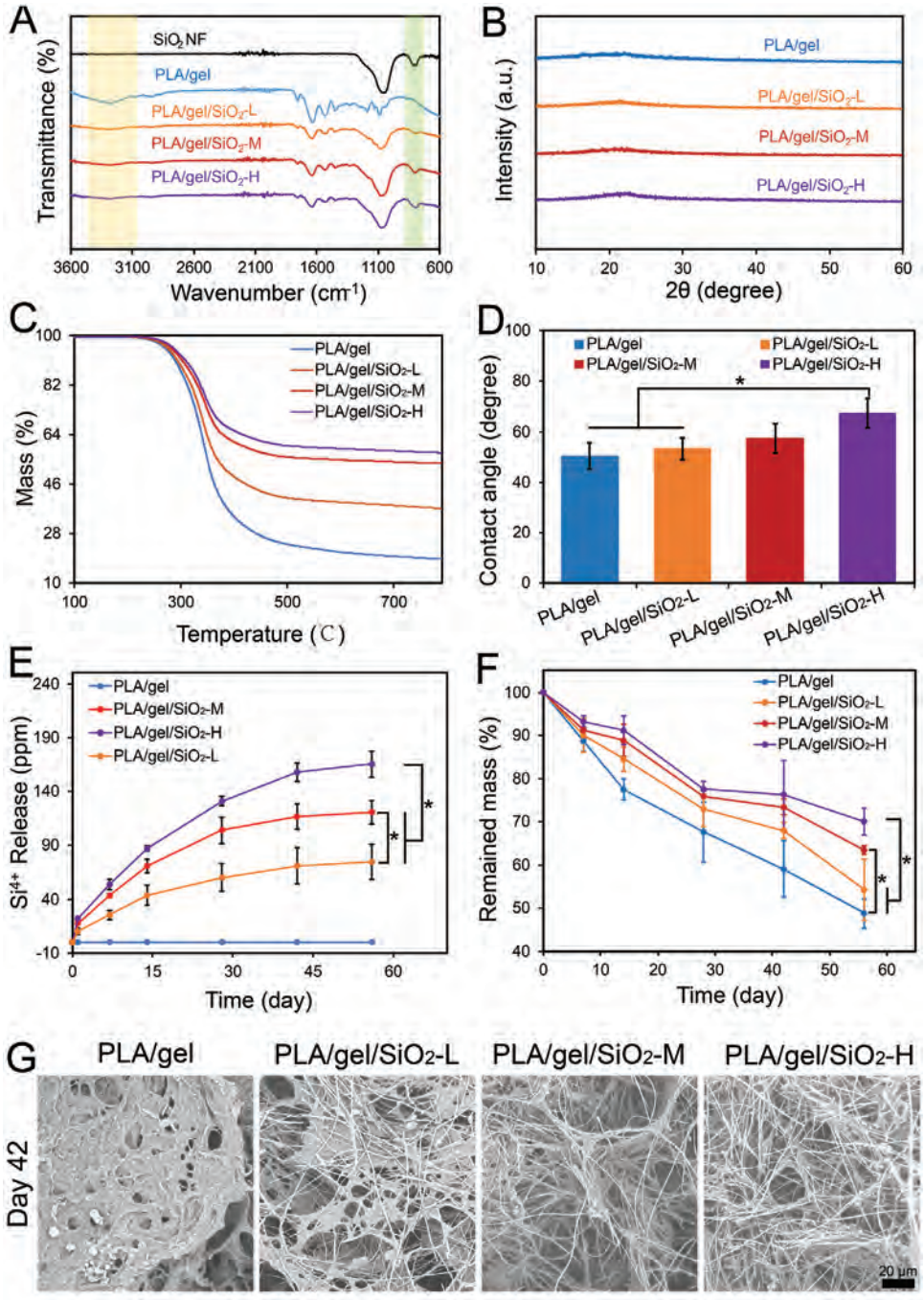

Figure 2. Physical and chemical properties of aerogel scaffolds. The FTIR spectra of SiO_2 nanofibers exhibited characteristic peaks at 802 and 1051 cm^{-1}, which can also be found in the FTIR spectra of aerogel scaffolds with different content of SiO_2 NF (A). In the XRD pattern (B), only a broad diffraction peak of gelatin appeared at $2\theta = 21.4°$. TGA analysis shows that the incorporation of SiO_2 nanofibers improved the thermal stability of the scaffold (C). The contact angle of aerogel scaffolds is about 40–80°, indicating that the aerogel scaffolds are hydrophilic (D). Cumulative release of silicon ions from aerogel scaffolds (E). It can be seen from the figure that silicon ions are released in a sustained fashion from scaffolds. After 8 weeks, the weight of the scaffolds had been reduced approximately by 30–50% (F). The SEM image of the scaffold incubated in PBS shows the morphology after 6 weeks (G). The statistical analysis is performed by the one-way analysis of variance of Tukey's post-hoc test, $n = 3–6$, and * means $p < 0.05$.

and 1540 cm^{-1}, respectively, which are ascribed to the gelatin, which can form amide bonds after thermal treatment.[25] The characteristic peaks of ester groups were located at 1185 and 1750 cm^{-1} corresponding to the C–O and C═O stretching vibration, respectively, indicating the chemical cross-linking between the PLA/gel nanofibers and the SiO_2 nanofibers (Figure S4, Supporting Information). The thermally crosslinked PLA/gel aerogel scaffolds failed to regain their original shape after repeated compression (Movie S1, Supporting Information). However, the PLA/gel/SiO_2-M aerogel scaffolds showed good elasticity after cross-linking, which could be beneficial to address the limitations associated with the brittle fracture of scaffolds. This good elasticity can be attributed to the incorporation of flexible SiO_2 nanofibers in the scaffold. The good flexibility of SiO_2 nanofibers can be attributed to two factors: 1) the reduction of nanofiber surface defects due to the amorphous nature of SiO_2 nanofibers and 2) amorphous SiO_2 nanofibers are less chemically constrained than that of the crystalline nanoparticles.[19] The XRD patterns of scaffolds further indicated their amorphous structure (Figure 2B). The thermal stability of aerogel scaffolds was evaluated by TGA as shown in Figure 2C. The initial degradation temperature of all groups was around 300 °C. These results indicate that the incorporation of SiO_2 nanofibers into PLA/gel did not influence the thermal stability of the aerogel scaffolds. The hydrophilicity of aerogels was determined by the water contact angle (WCA) test. As shown in Figure 2D, the aerogel scaffolds had WCA ranging from 50° to 70°, indicating that these aerogels are highly hydrophilic. The WCA of PLA/gel/SiO_2-H aerogel scaffolds showed an increasing trend with the decrease of gelatin amount. Since the hydrophilicity of aerogel scaffolds is attributable to the gelatin owning to its carboxylic (–COOH) and amino ($–NH_2$) groups; a reduction in the gelatin in aerogel scaffolds as a consequence of the addition of SiO_2 nanofibers may lead to a concomitant increase in the WCA.

Release of silicon ions (Si^{4+}) from scaffolds was examined for up to 56 days. While PLA/gel scaffolds lacked the release of Si^{4+} ions, PLA/gel/SiO_2 aerogel scaffolds showed a sustained release of Si^{4+}, which continued for up to 8 weeks (Figure 2E). At each time point, aerogel scaffolds containing higher SiO_2 content released significantly higher amount of Si^{4+}. The degradation of scaffolds was assessed in PBS for up to 8 weeks. PLA/gel aerogel scaffolds experienced significant degradation over time and lost approximately 50% of their mass by 8 weeks (Figure 2F). Similarly, the PLA/gel/SiO_2-L aerogel scaffolds showed a degradation curve similar to the PLA/gel aerogel scaffolds. In contrast, both PLA/gel/SiO_2-M and PLA/gel/SiO_2-H aerogel scaffolds had significantly slower degradation profiles compared with PLA/gel and PLA/gel/SiO_2-L scaffolds. Morphological analysis after 8 weeks revealed that PLA/gel/SiO_2 aerogel scaffolds maintained their structural stability and smooth fiber surface. In contrast, PLA/gel nanofibers were swollen and fused into solid matrix sheets, which resulted in the deformation of their porous structure (Figure 2G).

Figure 3A showed mechanical properties of scaffolds that were compressed for up to 90% in the dry state. It can be observed from the representative compressive stress-strain diagram that all samples obeyed Hooke's law in the initial stage of compression. The ultimate compressive strength (UCS) of the PLA/gel/SiO_2-M aerogel scaffolds was found to be 866.6 ±81.6 kPa, which was significantly higher than that of PLA/gel (683.3 ±116.9 kPa, $P = 0.02883$), PLA/gel/SiO_2-L (640 ± 89.4 kPa, $P = 0.00883$), and PLA/gel/SiO_2-H (516.7 ± 116.9 kPa, $P = 0.0000635$) aerogel scaffolds (Figure 3B). Similarly, PLA/gel/SiO_2-M scaffolds exhibited the highest compressive modulus as compared to the other scaffolds (Figure 3C). While PLA/gel, PLA/gel/SiO_2-L, and PLA/gel/SiO_2-H aerogel scaffolds displayed irreversible shrinkage, that did not return towards their original shapes, PLA/gel/SiO_2-M aerogel scaffolds regained their original shape and remained intact even after compressions (Figure 3D). The compressive properties of scaffolds were further measured in an aqueous environment, which manifested obvious differences between PLA/gel and PLA/gel/SiO_2 aerogel scaffolds. PLA/gel/SiO_2-M aerogel scaffolds exhibited superelasticity and regained their initial height under cyclic compression at a strain rate of 60% (Figure 3E). Compression of scaffolds for up to 1 cycle, 50 cycles, and 100 cycles was ascertained at 60% strain (Figure 3F–H). While PLA/gel and PLA/gel/SiO_2-L aerogel scaffolds underwent different degrees of plastic deformation, PLA/gel/SiO_2-H aerogel scaffolds fractured after 100 cycles. By contrast, PLA/gel/SiO_2-M aerogel scaffolds did not display plastic deformation or cracks even after repeated compressions for up to 100 cycles (Figure 3I). Quantitative analysis showed that the shape recovery rate of PLA/gel/SiO_2-M aerogel scaffolds was 94% and 91% after 50 and 100 cycles, respectively. According to photographs obtained by using optical microscope, PLA/gel, and PLA/gel/SiO_2-L aerogel scaffolds were compacted perpendicular to the direction of the fiber pore walls or channels of the stress, while the PLA/gel/SiO_2-H aerogels were collapsed, and the pore size became larger (Figure 3J). On the other hand, PLA/gel/SiO_2-M aerogel scaffolds still maintained their original porous structure. To demonstrate shape recovery rate, the compressed PLA/gel, and PLA/gel/SiO_2-M aerogels were immersed into water (Movie S2, Supporting Information); the compressed PLA/gel/SiO_2-M aerogels regained their original state within 3 s.

2.2. Cytocompatibility of PLA/gel/SiO_2 Aerogel Scaffolds

Cellular behaviors in terms of cell viability, morphology, and infiltration were assessed by live/dead staining and confocal laser microscopy. MC3T3-E1 cells, human umbilical vein ECs (HUVECs), and primary rat bone marrow-derived mesenchymal stem cells (rBMSCs) were cultured on scaffolds, which manifested good cell viability displaying only a few numbers of dead cells, thereby indicating the good cytocompatibility of scaffolds (**Figure 4**A). Quantitative analysis further revealed that the viable cell area was significantly higher in PLA/gel/SiO_2-M aerogel scaffolds than that of the other groups (Figure S6, Supporting Information). Confocal images revealed that while MC3T3-E1 cells were mainly accumulated on the surface of the PLA/gel scaffold, they were infiltrated into PLA/gel/SiO_2 scaffolds for up to various depths. Of PLA/gel scaffolds containing different content of SiO_2, the PLA/gel/SiO_2-M scaffolds supported the greatest cell infiltration with an even cell distribution than that of the other scaffolds (Figure 4B). In line with the confocal image observation, the quantitative assessment also confirmed that all of the three types of cells exhibited the greatest proliferation on the PLA/gel/SiO_2-M scaffold (Figure 4C–E).

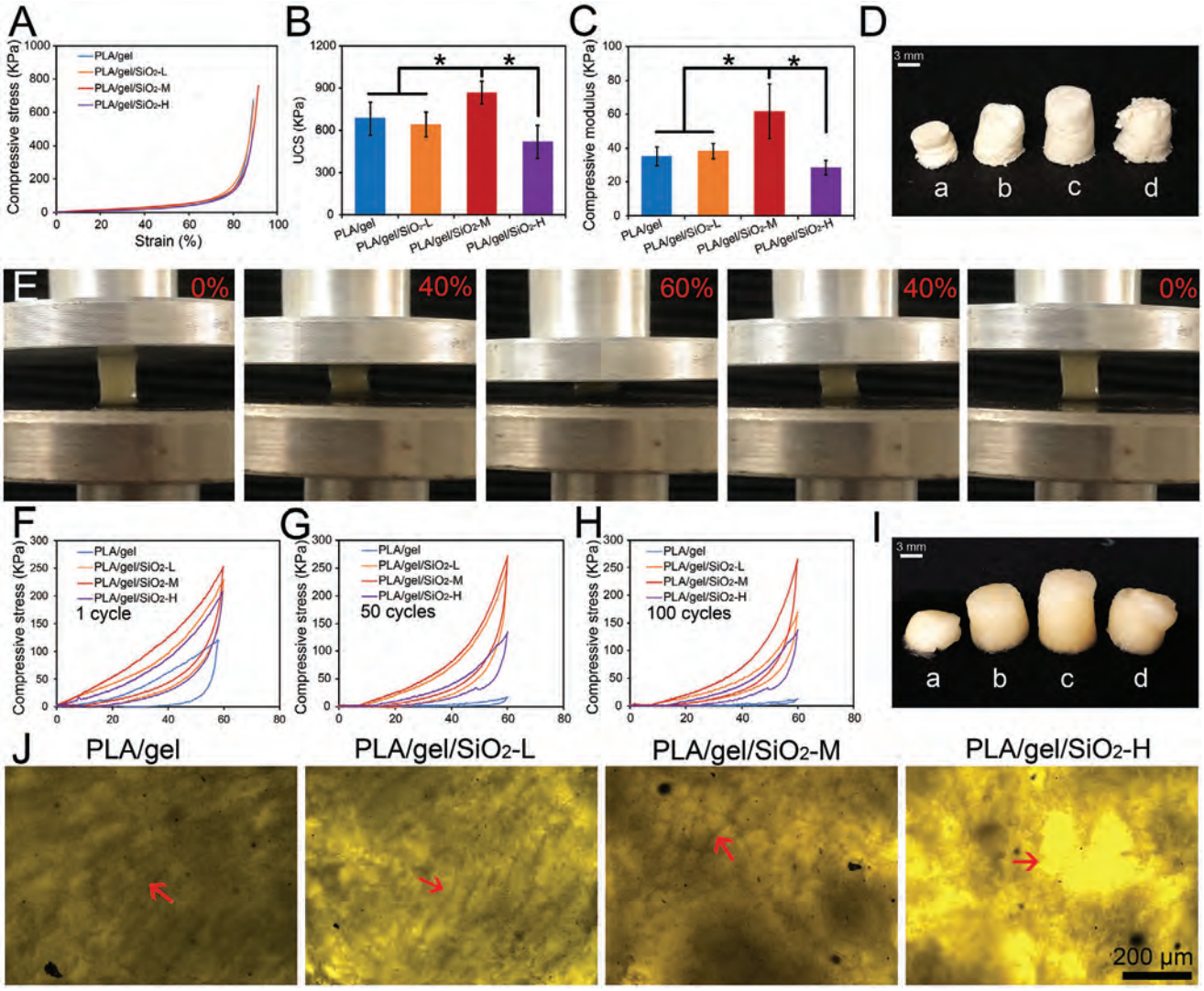

Figure 3. Compressive mechanical behavior of aerogel scaffolds with different SiO_2 nanofiber content. Under dry conditions, the PLA/gel/SiO_2-M group has greater compressive stress (A), UCS (B), and compressive modulus (C) as compared to the other scaffolds doped with SiO_2 nanofibers. Photographs of aerogel scaffolds after being compressed (D). (E) Macroscopic structural changes during compression and shape recovery in the aqueous medium. According to this compression method, (F) 1 cycle of compression, (G) 50 cycles of compression, and (H) 100 cycles of compression are performed on different wet scaffolds, respectively. Optical photographs showing changes in the macroscopic shape (I) (a) PLA/gel, (b) PLA/gel/SiO_2-L, (c) PLA/gel/SiO_2-M, (d) PLA/gel/SiO_2-H) and optical microscope images of internal microstructure (J) of hydrated aerogel scaffolds after 100 compressions. The statistical analysis is performed by the one-way analysis of variance of Tukey's post-hoc test, $n = 4$, and * means $p < 0.05$.

2.3. Collagen and VEGF Production

The quantification of collagen on scaffolds was performed by hydroxyproline assay. MC3T3-E1 cells showed progressively increased collagen deposition on the aerogel scaffolds for up to 10 days (Figure 4F). The PLA/gel/SiO_2-M scaffolds accumulated significantly higher content of collagen than that of the PLA/gel and PLA/gel/SiO_2-H scaffolds on day 10. Similarly, HUVECs responded to aerogel scaffolds containing SiO_2 NF; producing remarkably higher amount of VEGF on the PLA/gel/SiO_2-M scaffolds (Figure 4G). To further assess whether the PLA/gel/SiO_2 scaffolds can promote angiogenesis, we performed an in vitro tube formation assay by using HUVECs. PLA/gel/SiO_2 aerogel scaffolds promoted the tubule-like network formation of HUVECs (Figure S7A, Supporting Information). Quantitative analysis further revealed an obvious improvement in angiogenic parameters, including total length of tubules, number of junctions, number of meshes, and total mesh area on PLA/gel/SiO_2 scaffolds compared with the PLA/gel scaffolds; PLA/gel/SiO_2-M scaffolds outperformed other aerogel scaffolds (Figure S7B–E, Supporting Information).

2.4. Osteogenic Differentiation of rBMSCs

The osteogenic properties of aerogel scaffolds were assessed by quantifying alkaline phosphatase activity and accumulated calcified substrate by using alkaline phosphatase activity (ALP) and

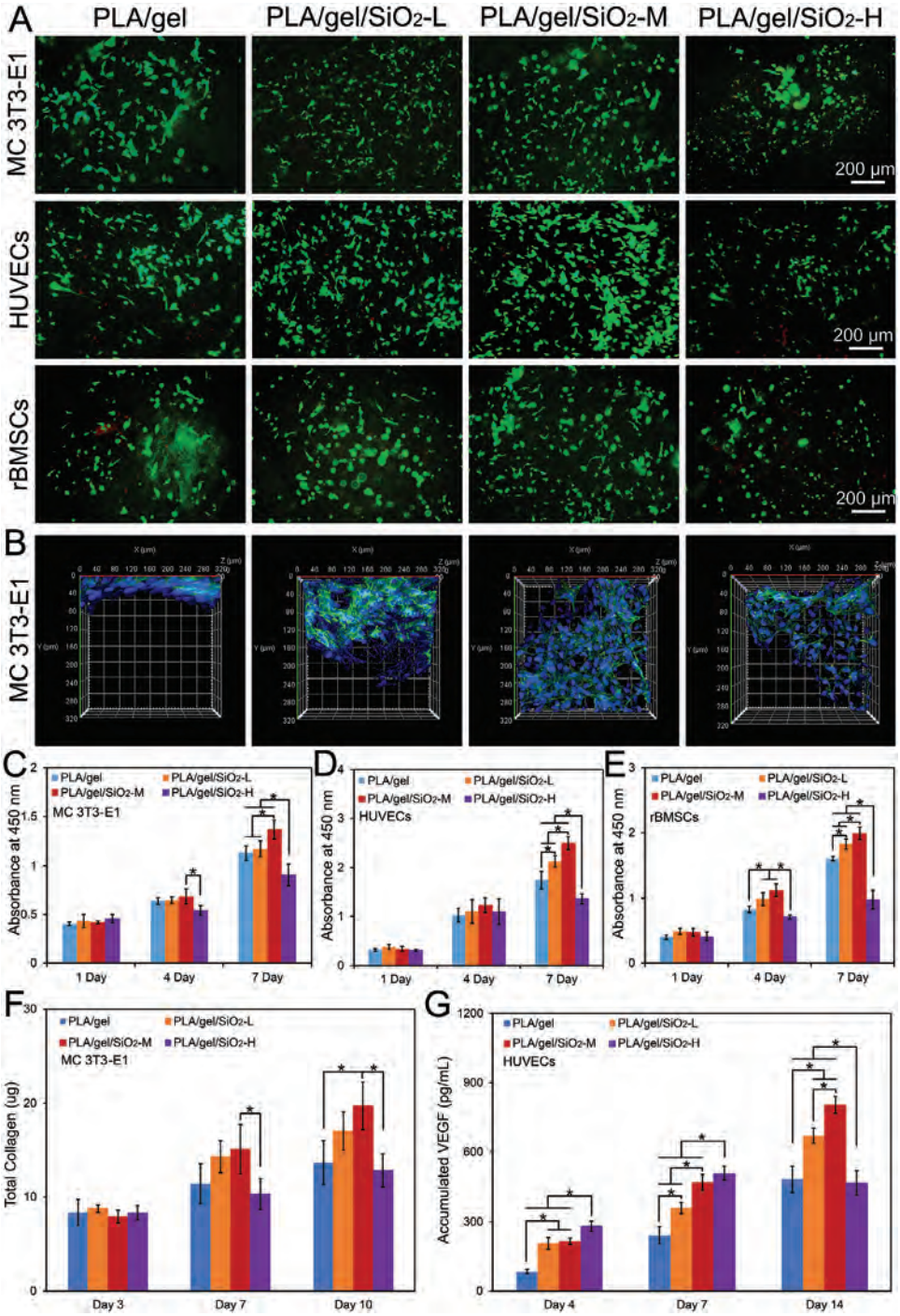

Figure 4. MC3T3-E1, HUVECs, and rBMSCs are used to evaluate the biocompatibility and cell morphology of different scaffolds. Live/dead staining (A) after seven days showed that compared with the other scaffolds, the PLA/gel/SiO_2-M scaffolds had significantly more live cell population (green). The confocal laser microscopy (B) is used to evaluate the growth of cells in the scaffolds. The CCK-8 assay also semi-quantitatively indicated that the scaffolds incorporating an appropriate proportion of SiO_2 nanofibers can promote cell proliferation. MC3T3-E1 (C), HUVECs (D), and rBMSCs (E). The amount of collagen accumulated in the co-culture of MC3T3-E1 and aerogel scaffolds (F). The amount of VEGF accumulated by co-cultivating HUVECs on aerogel scaffolds (G). The statistical analysis is performed by using one-way analysis of variance of Tukey's post-hoc test, $n = 4$, and * means $p < 0.05$.

Alizarin Red S (ARS) staining, respectively. The PLA/gel/SiO_2-M scaffolds showed the strongest purple color among all of the aerogel scaffolds on day 14 (**Figure 5**A). Quantitative analysis of ALP demonstrated that rBMSCs seeded on the PLA/gel/SiO_2-M scaffold had significantly higher ALP activity compared with the other scaffolds (Figure 5B). ARS assay further showed that PLA/gel/SiO_2 scaffolds promoted biomineralization, which was the highest in the PLA/gel/SiO_2-M scaffolds among all groups (Figure 5C,D). To gain further insight into the underlying molecular mechanism of higher osteogenic differentiation on aerogel scaffolds containing SiO_2 nanofibers, we cultured rBMSCs on PLA/gel and PLA/gel/SiO_2-M scaffolds and evaluated the expression levels of osteogenic genes by real-time quantitative PCR (RT-qPCR) at day 4, 7, and 14 after cell culture. As can be seen from Figure 5, PLA/gel/SiO_2-M scaffolds expressed significantly higher levels of osteogenic genes than that of their counterparts devoid of SiO_2 nanofibers. We found that Run-related transcription factor 2 (RUNX-2) and bone morphogenetic protein 2 (BMP-2) were highly expressed at the earlier and middle stages of osteogenic differentiation (Figure 5E,G). On the other hand, the expression level of the collagen type 1 (Col-1) was the highest on day 4, which decreased thereafter (Figure 5F). The osteopontin (OPN), an osteogenic marker expressed at the later stages of osteogenic differentiation was the highest on day 14 (Figure 5H). Western blot analysis was performed to assess whether the PLA/gel/SiO_2-M scaffolds could promote the expression of osteogenic proteins (Figure 5I). The quantitative analysis showed that the PLA/gel/SiO_2-M aerogel can promote the expression of RUNX-2 and OPN proteins in rBMSCs (Figure 5J,K). These results indicate that the SiO_2 nanofibers can up-regulate the expression of osteogenic genes and proteins, which may also have implications for bone tissue regeneration in vivo.

2.5. In Vivo Evaluation of Scaffolds

The osteo-inductive ability of PLA/gel and PLA/gel/SiO_2-M scaffolds was further ascertained after implantation in a calvarial defect model in rats for up to 12 weeks. **Figure 6**A showed micro-computed tomography (Micro-CT) images of calvarial defects 4, 8, and 12 weeks post-operative surgical operation (Figure 6). Green areas represented newly formed bone tissues. The quantitative analysis of the new bone coverage distinctly revealed that the PLA/gel/SiO_2-M scaffold had reached 93% by the 12th week (Figure 6B). The bone volume to total tissue volume (BV/TV) of the PLA/gel/SiO_2-M aerogel scaffolds was also significantly higher than that of the control and PLA/gel aerogel scaffold groups (Figure 6C). The bone mineral density (BMD) of PLA/gel/SiO_2-M (0.213 ± 0.022 g cm^{-3}) was also significantly higher as compared to the PLA/gel group (0.131 ± 0.009 g cm^{-3}) and control group (0.097 ± 0.007 g cm^{-3}) (Figure 6D).

The regenerative potential of PLA/gel and PLA/gel/SiO_2-M aerogel scaffolds was assessed in a calvarial defect model in rats for up to 12 weeks in vivo. Histological analysis by hematoxylin and eosin (H&E) staining on decalcified tissues was performed (Figure 6E,F). Both types of scaffolds lacked inflammatory cell recruitment. PLA/gel/SiO_2-M group exhibited the formation of new bone by the 8th week. By contrast, the control and PLA/gel groups had only a small amount of new bone formation. Similarly, Masson's trichrome staining revealed the faster bone formation rate in the PLA/gel/SiO_2-M group as compared to the other groups. Thereafter, immunofluorescence staining for endothelial marker "CD31" and the vascular smooth muscle marker alpha-smooth muscle actin (α-SMA) was performed to delineate angiogenic effect of silicon ions released by PLA/gel/SiO_2-M aerogel scaffold during bone repair. As shown in **Figure 7**A, the control and PLA/gel groups showed only a few numbers of CD31/α-SMA-positive blood vessels at the earlier stages of bone repair (i.e., 4th week). By contrast, large numbers of CD31/α-SMA-positive blood vessels were found at the edges and center of the defect in the PLA/gel/SiO_2-M aerogel scaffolds. The quantitative analysis further showed significantly higher $CD31^+$ and α-SMA^+ area in the PLA/gel/SiO_2-M aerogel scaffold than that of the control and PLA/gel groups (Figure 7C,D). We also performed immunofluorescence staining for osteoblast markers, including OPN and osteocalcin (OCN) (Figure 7B). The expressions of OCN and OPN in the PLA/gel/SiO_2-M group were significantly higher than that of the control and PLA/gel groups. The quantitative analysis also showed significantly higher OCN^+ and OPN^+ areas in PLA/gel/SiO_2-M aerogel scaffold group than that of the other groups (Figure 7E,F). Overall, these results indicate that scaffolds containing flexible SiO_2 nanofibers can simultaneously induce angiogenesis and osteogenesis, which may have broad implications for bone tissue regeneration.

3. Discussion

The treatment of bone defects is very important to maintain the patient's physical integrity.[26] So far, scaffold-based tissue engineering approaches have been widely exploited to treat critical-sized bone defects owning to their obvious advantages. However, irregular-shaped bone defects are difficult to be managed by the scaffold-based approach due to the limitations associated with the scaffolds' dimensions and adaptability at the implantation site. For the treatment of complex bone defects, scaffolds need not only to mimic the bone microenvironment, but they also need to induce osteogenesis and angiogenesis. Additionally, for irregular bone defects, scaffolds should be minimally invasive and adaptive to realize the osseointegration of irregular bone defects.[27] Parallelly, wear debris produced by the erosion of bone implants poses inflammation and implant failure risks. The poor integration between the bone-implant and host tissues may lead to bone resorption and osseointegration.[28] Recently, aerogel scaffolds have garnered considerable interest in the research community for the treatment of irregularly-shaped tissue defects in an array of regenerative medicine and tissue engineering applications. We and other groups have previously demonstrated that electrospun nanofiber aerogel scaffolds possess excellent elasticity and flexibility, which endow them with the shape-memory for filling irregular-shaped tissue defects. For instance, we showed that electrospun PLA/gel aerogels functioned well as self-fitting scaffolds, which intimately filled articular cartilage defects and promoted cartilage regeneration.[15] This self-fitting capability was further extended to the hard tissues where electrospun PLA/gel aerogel scaffolds were shown to closely fill the cranial defects, however, they lacked bone regeneration.[23] We speculate that the poor regenerative capability of scaffolds may be associated due to the poor mechanical stability and fast degradation of scaffolds.

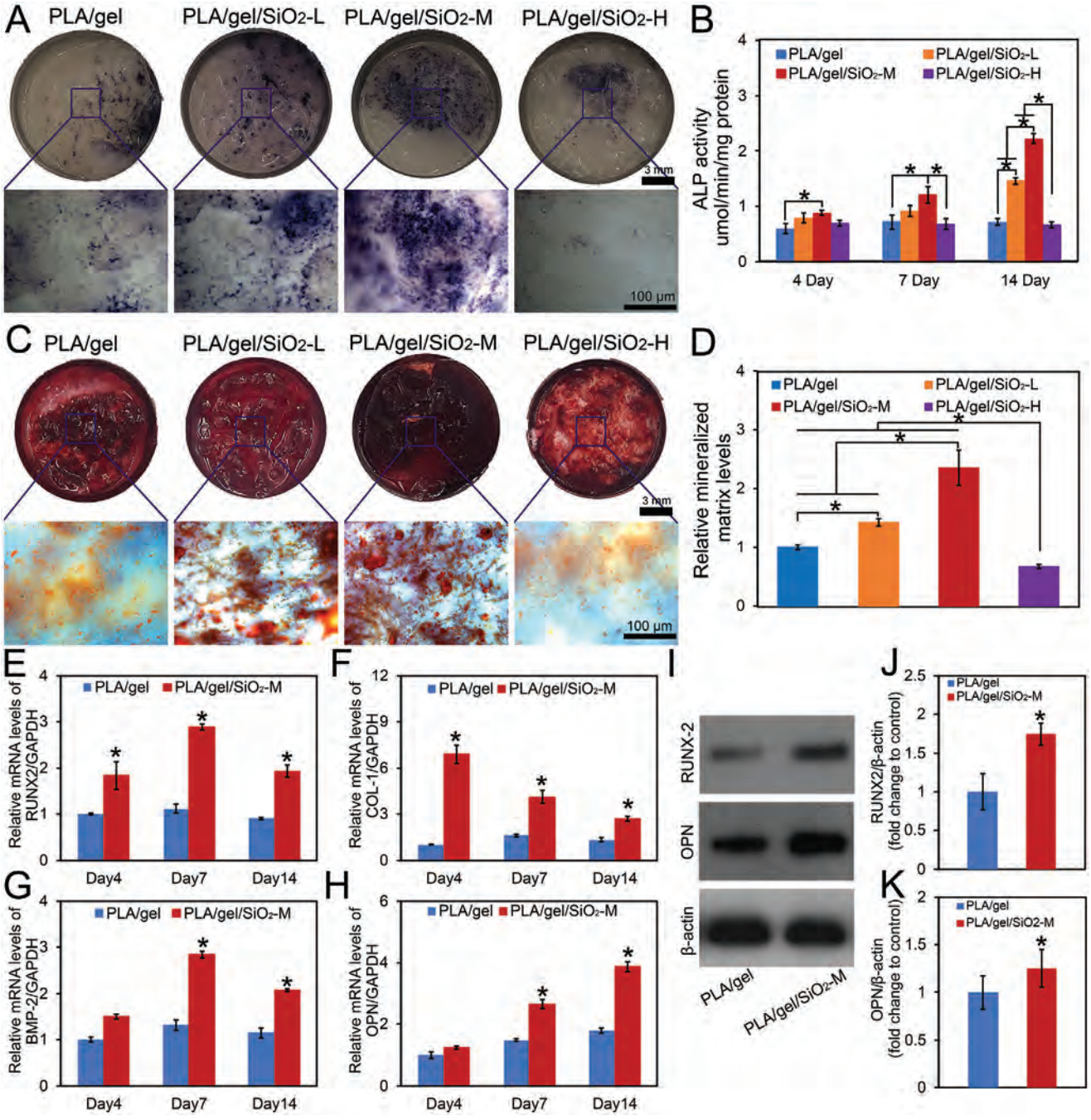

Figure 5. rBMSCs are cultured on aerogel scaffolds to evaluate their osteogenic differentiation ability. Alkaline phosphatase staining (A) and alkaline phosphatase activity (B). Alizarin Red S staining (C) detected calcium deposition of rBMSCs on the aerogel scaffolds. Quantitative analysis of the results obtained by Alizarin Red S staining showing the calcium deposition on the aerogel scaffolds (D). Osteogenic differentiation experiments indicated that the osteogenic ability of the PLA/gel/SiO_2-M scaffold is higher than that of the other groups. The statistical analysis is performed by one-way analysis of variance of Tukey's post-hoc test, $n = 3$–4, and * means $p < 0.05$. Expression of RUNX-2 (E), Col-1 (F), BMP-2 (G), and OPN (H) of rBMSCs co-cultured with PLA/gel scaffold and PLA/gel/SiO_2-M scaffold. Osteogenic protein expression in rBMSCs cultured on PLA/gel and PLA/gel/SiO_2-M scaffold: Western blot analysis (I) for the detection of osteogenic protein. Semi-quantitative analysis of OPN (J) and RUNX-2 (K). Unpaired Student's *t*-test, * indicates $p < 0.05$ versus PLA/gel.

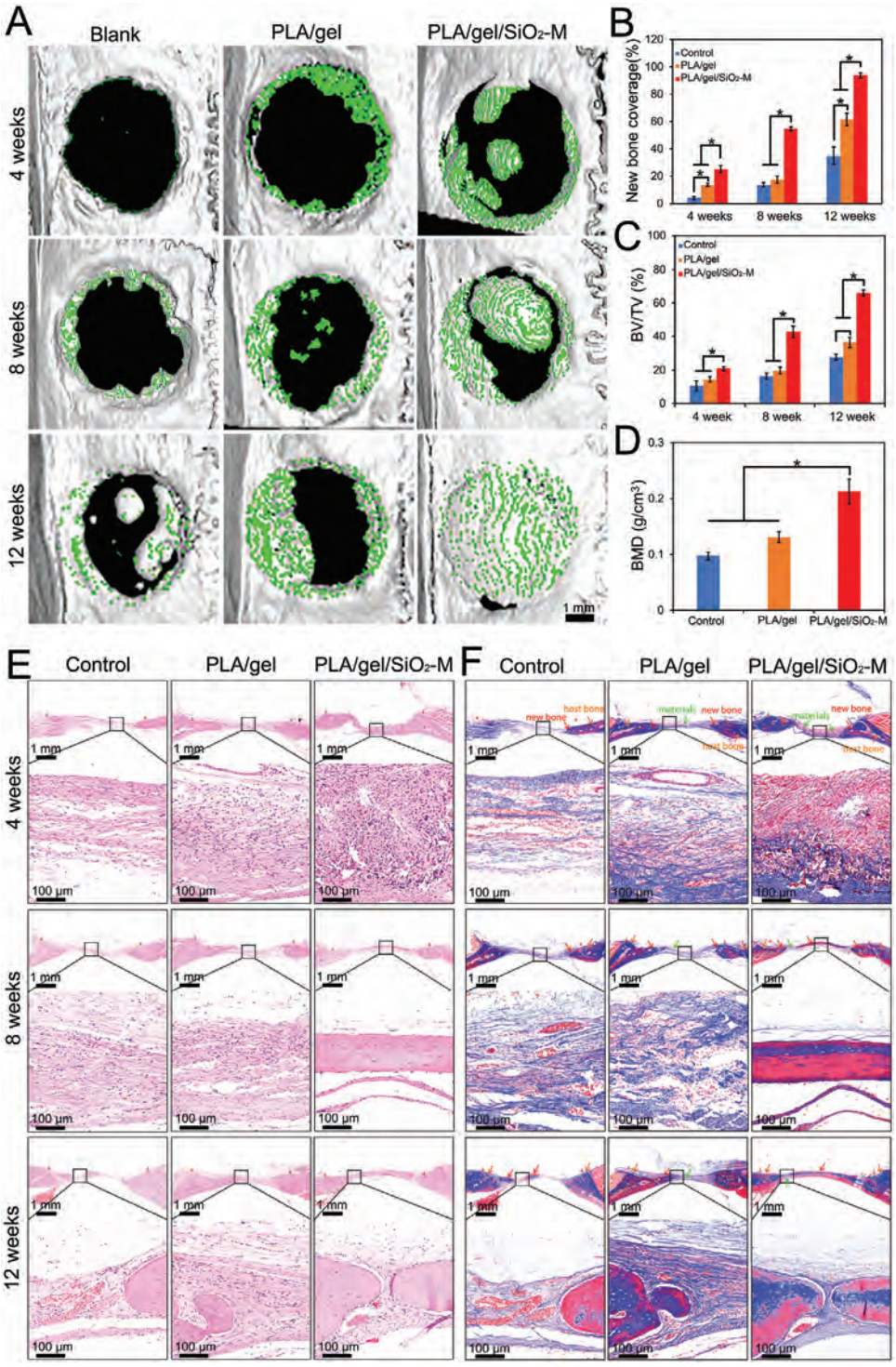

Figure 6. Assessment of aerogel scaffolds in a calvarial defect model in rats for up to 12 weeks in vivo. Photographs obtained from micro-computed tomography (Micro-CT) (A) of the calvarial defect model in rats at different time points (the green part indicated the new bone). The coverage rate (B) of new bone area in the calvarial defect area at different time points. The volume fraction (C) of new bone in the calvarial defect area at different periods. The BMD (D) of the skull defect area at 12 week post-operatively. H&E staining (E) and Masson's trichrome staining (F) are performed on the decalcified tissues 4, 8, and 12 weeks post-operatively. The statistical analysis is performed by using one-way analysis of variance followed by Tukey's post hoc test. $n = 4$, * indicated $p < 0.05$.

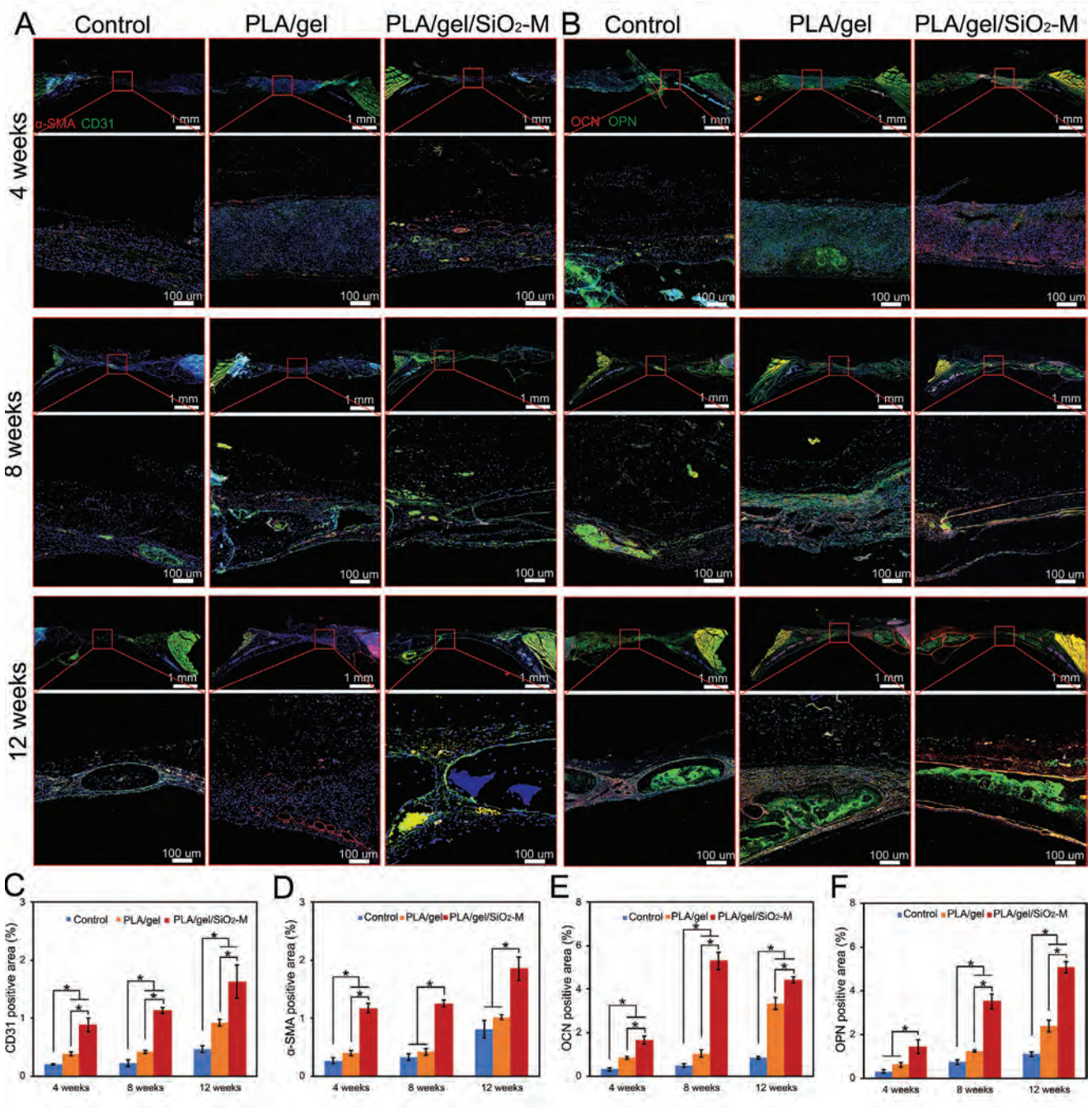

Figure 7. Immunofluorescence staining explanted scaffolds are performed 4, 8, and 12 weeks post-operatively. A) Sections are stained with CD31 (red) and α-SMA (green). B) Immunofluorescence staining of scaffolds by using OCN (red) and OPN (green). C–F) Quantitative analysis of positively stained areas is performed by using Image-Pro Plus software. The statistical analysis is carried out by using one-way analysis of variance by employing Tukey's post hoc test. $n = 4$, * means $p < 0.05$.

To verify this hypothesis, we subcutaneously implanted PLA/gel aerogel scaffolds in a rat model. Our results showed that the PLA/gel aerogel scaffolds easily lost their porous structure and deformed into a mass of dense nanofibers within two weeks of implantation (Figure S5, Supporting Information). Biomineralization represents an effective approach to improve the structural stability of electrospun aerogel scaffolds. During mineralization, a large amount of calcium phosphate is deposited on the surface of nanofibers, which profoundly increases the rigidity of aerogel scaffolds.[29] Despite improved mechanical properties, biomineralized aerogel scaffolds show compromised shape-memory capability, which abrogates their conformal fitting ability for filling irregular-shaped defects. Alternatively, the introduction of rigid nanofibers to aerogels might circumvent this problem.

Electrospun SiO_2 nanofibers represent a good candidate for this purpose because of their multiple features, such as good flexibility, rigidity, and osteogenic activity.[19] Consequently, we combined electrospun SiO_2 nanofibers and PLA/gel nanofibers to prepare aerogel scaffolds with superelasticity and good stability.

Appropriate crosslinking methods for PLA/gel/SiO_2 aerogel scaffolds are of pivotal importance to further ensure their physicochemical properties and biological performance. Chemical crosslinking agents, including glutaraldehyde,[30] 1-ethyl-3-(3-dimethyl aminopropyl) carbodiimide (EDC)/*N*-hydroxysuccinimide (NHS),[31] and genipin[32] have been extensively employed for the crosslinking of electrospun aerogel scaffolds. In spite of their good crosslinking effectiveness, the potential cytotoxicity of these chemical agents might limit their applicability.[19] Therefore, it is of significance to exploit a non-toxic approach to cross-link PLA/gel/SiO_2 aerogel scaffolds. Electrospun SiO_2 nanofibers are featured by the hydroxyl groups on their surface, which could be induced to react with many active groups. Previously, we and other groups have shown that PLA/gel nanofibers can be crosslinked through thermally-induced dehydration and condensation between the carboxylic and amino groups. Theoretically, hydroxyl groups of SiO_2 nanofibers can react with the carboxylic groups via dehydrative condensation. Therefore, we exploited thermal treatment by annealing PLA/gel/SiO_2 aerogel scaffolds at 190 °C for 2 h. Crosslinking of scaffolds by thermally-induced dehydrative condensation between hydroxyl groups of SiO_2 nanofibers and the carboxylic groups of PLA/gel nanofibers was confirmed by the presence of ester groups as revealed by FTIR (Figure 2A). The SiO_2 nanofibers and the carboxyl groups on the surface of the scaffolds were chemically bonded. The combination of groups rendered the aerogel scaffolds with good structural stability and flexibility.

Therefore, the mechanical properties of the PLA/gel/SiO_2-M aerogel scaffolds were significantly higher as compared to the PLA/gel aerogel scaffolds (Figure 3A). However, with an increase in SiO_2 content, the combination of functional groups may become difficult, rendering the crosslinking to be insufficient. Consequently, PLA/gel/SiO_2-H aerogel scaffolds exhibited poor structural stability than that of their counterparts containing low content of SiO_2 nanofibers (Figure 3D). These results indicated that the mechanical properties of the PLA/gel/SiO_2-L aerogel scaffolds may reach an appropriate level even at the low content of SiO_2 nanofibers due to their insufficient rigidity. However, once the content of SiO_2 nanofibers reached up to 60%, the mechanics of the PLA/gel/SiO_2-H aerogel scaffolds became worse due to the insufficient cross-linking among the fibers. Therefore, once the mass ratio between SiO_2 nanofibers and PLA/gel nanofibers reached 4:6, the aerogel scaffolds can be fully crosslinked. In an aqueous environment, the PLA/gel/SiO_2-M aerogel scaffolds exhibited superelasticity and completely regained their initial height at a strain rate of 60% during cyclic compression test, indicative of a porous structure with good fatigue resistance (Figure 3I). Furthermore, the PLA/gel/SiO_2-M aerogel scaffolds were expanded in volume after absorbing water, which revealed that they can better fit the edge of the defect and provide a conducive environment for cell growth (Figure S9, Supporting Information). Subcutaneous implantation showed good structural stability of PLA/gel/SiO_2-M aerogel scaffolds as compared to PLA/gel aerogel scaffolds. From H&E staining (Figure S8, Supporting Information), it was found that the PLA/gel/SiO_2-M aerogel scaffolds can maintain their 3D porous structure for up to 14 days. At the same time, it was found that cells can rapidly proliferate in the PLA/gel/SiO_2-M aerogel scaffolds and grow uniformly into the scaffolds to promote tissue regeneration.

SEM and EDS images showed that the SiO_2 nanofibers were uniformly distributed in the aerogel scaffolds. The crosslinked PLA/gel aerogel scaffolds revealed a sheet-like structure. In contrast, PLA/gel/SiO_2 aerogel scaffolds displayed a fluffy and porous structure due to the stronger rigidity of SiO_2 nanofibers. The 3D porous structure may not only provide proper oxygen and nutrients for cells but may also effectively remove metabolites during cell proliferation. This endows a suitable microenvironment for neovascularization and bone formation.[13] Subsequently, we evaluated the release of silicon ions as well as the degradation of PLA/gel/SiO_2 aerogels scaffolds (Figure 2). PLA/gel aerogel scaffolds rapidly lost their mass in vitro, which may not be conducive for their in vivo application as they will undergo structural deformation prior to tissue regeneration. Notably, the addition of SiO_2 nanofibers prolonged the degradation of PLA/gel/SiO_2 aerogel scaffolds, permitting the sustained release of silicon ions. The important role of silicon in stimulating cell proliferation and inducing osteogenic differentiation has been reported previously, including those related to the calcium silicate,[33] silica apatite cement,[34] silicate bioceramics,[21a] and silicon-containing bioglass.[35] PLA/gel/SiO_2 aerogel scaffold promoted cell growth in vitro.

Composite nanofiber materials can adjust cell density and osteogenic differentiation by adjusting the ratio of inorganic and organic components.[36] In the osteogenic induction experiment in vitro, the detection and evaluation of ALP (Figure 5A) and ARS (Figure 5C) showed that the expression and degree of mineralization of the bone protein of PLA/gel/SiO_2-M aerogel scaffold were significantly higher than that of the other groups. The poor biological activity of PLA/gel/SiO_2-H aerogel scaffold may be due to the high content of SiO_2 nanofibers, which may have reduced the biological activity of the aerogel scaffold.[30]

The PLA/gel/SiO_2 aerogel scaffolds not only have strong mechanical properties but also promote angiogenesis and osteogenic differentiation of rBMSCs, which may have implications for bone repair in vivo. During bone repair, the neovascularization is particularly important. Insufficient vascular networks often lead to hypoxia and necrosis of tissues, which in turn leads to failure of bone repair.[13] The role of blood vessels is to mainly provide nutrients and oxygen to cells, which is essential for the bone regeneration process. Previous studies have found that the insufficient vascularization reduced bone formation.[37] The silicon ions released from the PLA/gel/SiO_2 aerogel scaffold promoted the expression of VEGF in HUVECs (Figure 4G), thereby promoting angiogenesis and bone regeneration.

The osteogenic differentiation process is divided into three different stages, including cell senescence, matrix maturation, and finally mineralization. In the early stages of differentiation, rBMSCs slowly express osteoblast-type genes, such as COL-1, OCN, and RUNX-2. One of the earliest features of osteoblast differentiation is the expression of RUNX-2,[38] which is an important mediator of the osteoblastic differentiation.[39] The expression level of RUNX-2 was the highest on day 7, which decreased thereafter.

On the other hand, the OPN is abundantly expressed in the late stage of osteogenic differentiation. The expression levels of the osteoblast-type genes were significantly higher in PLA/gel/SiO_2-M aerogel scaffolds than that of the PLA/gel aerogel scaffolds during the entire culture period. In summary, the PLA/gel/SiO_2-M aerogel scaffolds displayed a regulatory effect on the osteogenic differentiation of rBMSCs.

PLA/gel/SiO_2-M aerogel scaffolds also displayed significantly higher blood vessel regeneration and osteogenic differentiation in vivo as compared to the PLA/gel aerogel scaffolds in a rat calvaria defect model in vivo, which further confirmed the beneficial effects of SiO_2 nanofibers on angiogenesis and osteogenesis. A significantly higher expression of $CD31^+$ and a-SMA^+ area in PLA/gel/SiO_2-M aerogel scaffold than that of the control, and PLA/gel groups indicated the stimulatory effect of silicon ions on angiogenesis (Figure 7A). We envision that the cells can communicate with each other due to the porous structure of the scaffolds. Immunofluorescence staining for (Figure 7B) OPN and OCN further confirmed that the PLA/gel/SiO_2-M aerogel scaffolds enhanced the expression of OPN and OCN during bone formation. It can be seen from Figure 6A that the new bone area of the PLA/gel/SiO_2-M aerogel scaffold is larger than that of the PLA/gel aerogel scaffold and the control group. These results indicate that the silicon ions released from the PLA/gel/SiO_2-M aerogel scaffolds along with a porous nanofibrous structure can promote vascularization, which is a key step in bone regeneration.

In summary, we have demonstrated the preparation of superelastic 3D porous organic/inorganic composite nanofiber scaffolds by thermal crosslinking. PLA/gel/SiO_2-M scaffolds not only displayed shape memory but also exhibited good mechanical properties. Due to their porous 3D-like nanofibrous structure, PLA/gel/SiO_2-M scaffolds provided a conducive environment for cell growth in vitro and in vivo as well as simultaneously induced angiogenesis and osteogenesis. The silicon ions released by the scaffolds can promote the paracrine function between rBMSCs and HUVECs, further promoting vascularization and osteogenesis as well as providing cells with sufficient oxygen and nutrients. This study has also limitations. For example, we have not elucidated the inhibitory effect of the higher concentration of SiO_2 on cellular processes in vitro and in vivo. Similarly, we employed calvarial defect model in rats, which may not accurately reflect the bone microenvironment. The evaluation of these scaffolds is therefore warranted in irregular-shaped complex bone defects.

4. Conclusions

In summary, we developed an elastic 3D porous organic/inorganic composite nanofibrous aerogel scaffold with interconnected open porous structure to mimic the morphological structure of bone ECM and leverage silicon ions to induce osteogenesis and angiogenesis for bone regeneration. Scaffolds containing 40% (w/w) of short SiO_2 nanofibers exhibited significantly higher mechanical properties and mechanical elasticity. In vitro studies showed that the PLA/gel/SiO_2-M aerogel scaffolds not only displayed significantly higher cell survival rate, but also promoted osteogenic differentiation of rBMSCs. PLA/gel/SiO_2-M scaffolds also promoted bone regeneration in a calvarial defect model in rats for up to 12 weeks as compared to the defect only or PLA/gel groups. Taken together, these composite 3D porous aerogel scaffolds containing flexible SiO_2 nanofibers induced the differentiation of rBMSCs into osteoblasts and promoted bone repair, which may have broad implications for tissue engineering.

5. Experimental Section

Materials: PLA (Jinan Daigang Biomaterial; DG-L150) and type A gelatin (≈300 g Bloom) were purchased from Sigma-Aldrich. Hexafluoroisopropanol (HFIP, Aladdin Chemistry; H107501), TEOS (Sigma-Aldrich), H_3PO_4 (Shanghai Lingfeng Chemical reagent Co., LTD), and polyvinyl alcohol (PVA, Aladdin, $M_n = 86$ kDa) were used as received without any further purification.

Preparation and Characterization of PLA/gel/SiO_2 Aerogel Scaffolds: The detailed preparation methods of PLA/gel nanofiber membrane and flexible SiO_2 nanofiber membrane are provided in the Supporting Information. PLA/gel/SiO_2 composite nanofiber aerogel scaffolds were fabricated as follows: PLA/gel nanofibers and SiO_2 nanofibers were cut into pieces of about 1 cm × 1 cm. About 2.5 g of nanofibers pieces with or without SiO_2 nanofibers were mixed with 100 mL of tertiary-butyl alcohol and homogenized by using a high-speed mixer (IKA T18, Germany) at 15 000 rotations per min (rpm) for up to 30 min to afford homogenous dispersion of nanofibers fragments. The SiO_2 content were varied from 0–60% (w/w) to produce composite scaffolds containing 0, 20, 40, and 60% (PLA/gel, PLA/gel/SiO_2-L, PLA/gel/SiO_2-M, and PLA/gel/SiO_2-H, respectively) of SiO_2 nanofibers. Thereafter, the nanofiber mixture was poured into the wells of the 96-wells plates and placed in a refrigerator at −80 °C for 12 h followed by freeze-drying for 72 h to afford uncrosslinked 3D aerogel scaffolds. Different uncrosslinked 3D aerogel scaffolds were placed in a muffle furnace at 190 °C for up to 2 h to obtain crosslinked aerogel scaffolds. Surface morphology and chemical compositions of PLA/gel/SiO_2 aerogel scaffolds were analyzed by scanning electron microscopy (SEM, Hitachi, TM-1000, Japan) with an ESM spectrometer. The structural elucidation of SiO_2 nanofibers and PLA/gel/SiO_2 aerogel scaffolds were further performed by FTIR and X-ray diffraction (XRD). Samples were scanned in the range of 3600–600 cm^{-1} by using Nicolet-760 FITR spectrophotometer. For XRD analysis, X-ray diffractometer (AXS D8 Discover, Brukers) was used to detect the structure of samples in the range of $2\theta = 10$–60°. Thermal stability of aerogel scaffolds was assessed in an inert atmosphere by using thermogravimetric analyzer (a Libra 209F1, Selb, Germany). Samples were scanned from 100 °C up to 800 °C at a scan rate of 10 °C min^{-1}. The contact angle of scaffolds was measured by a contact angle analyzer (SL200A, Solon Tech., Shanghai, China). Deionized water (5 µL) was dropped onto the surface of aerogel scaffolds and imaged until the droplet disappeared. Images at 5 s were extracted from videos to calculate the contact angle ($n = 6$ for each group).

The release of Si ion from aerogel scaffolds ($n = 4$ for each group) (diameter, 14 mm, thickness, 1 mm) was assessed after immersion in 0.9% saline at 37 °C for up to different time points. At pre-determined time point, the solution was collected and an equal volume of the fresh solution was added. The concentration of the released silicon ions was determined by inductively-coupled plasma-atomic emission spectroscopy (ICP-AES, Prodigy Plus, Teledyne Leeman Labs, USA).

The degradation of aerogel scaffolds was performed in phosphate-buffered saline (PBS) at 37 °C in vitro. The aerogel scaffolds were weighed (m_0) and immersed into PBS. At pre-determined time points, samples were retrieved, lyophilized, and weighed (m_t) ($n = 3$ for each group). The degradation rate of aerogel scaffolds was expressed in terms of the percentage of remaining mass and was calculated as follows:

$$\text{Percentage of remained mass (\%)} = m_t/m_0 \times 100\% \quad (1)$$

Where m_0 and m_t represent the mass of samples at day 0 and at a predetermined time point.

To observe the fibrous structure of aerogel scaffolds by using SEM after degradation, samples were thoroughly rinsed with deionized water, lyophilized, and sputtered-coated with gold. The morphology of scaffolds after degradation was analyzed by scanning electron microscopy (SEM, Hitachi, TM-1000, Japan).

A universal material testing machine (Instron 5567, Norwood, MA) was used to evaluate the compressive mechanical properties of cylindrical aerogel scaffolds under dry and wet conditions (diameter, 6 mm). For dry conditions, the aerogel scaffolds were compressed for up to 90% of their deformation at a compression rate of 5 mm min^{-1}. The UCS was determined by the maximum compressive strength from compression to 90% of their deformation. Young's modulus was calculated from the stress-strain curve as the slope of the initial 10% linear region ($n = 4$ for each group). For wet conditions, 1, 50, and 100 cycles of loading-unloading fatigue tests were performed by measuring 60% compressive strain at a compression speed of 10 mm min^{-1}. The samples were hydrated with PBS at 37 °C before testing. After fatigue tests, the surface morphology of samples was observed by using a microscope (DMi 8, Leica, Germany).

Cytocompatibility of Scaffolds: MC3T3-E1 (ATCC, provided by the Cell Bank of the Chinese Academy of Sciences), HUVECs (Cell Bank of the Chinese Academy of Sciences), and rBMSCs (isolated from SD rats) were used following the previous reports[40] to evaluate the cytocompatibility of scaffolds. The further details of methods have been listed in Supporting Information.

Quantification of Collagen and VEGF: The collagen deposition by MC3T3-E1 cells on the aerogel scaffolds was measured by hydroxyproline assay. The aerogel scaffolds seeded with MC3T3-E1 cells were hydrolyzed in 3 M sulfuric acid at 105 °C for 2 h, and then cooled to room temperature. The hydrolyzed solution was incubated with the chloramine T solution at room temperature for 20 min, and then incubated with the color reagent at 65 °C for 20 min. Thereafter, the absorbance of solution was recorded by Multiskan MK3 microplate reader at 558 nm ($n = 4$ for each group). A standard calibration curve of hydroxyproline with different concentration gradients was prepared to calculate the amount of hydroxyproline in each sample.

HUVECs were seeded on aerogel scaffolds in a 24-well plate at a density of 1×10^5 cells per well. The cell culture supernatant was collected and stored at −80 °C on days 4, 7, and 14. The VEGF content was measured by using VEGF enzyme-linked immunosorbent assay (ELISA, Cusabio; CSB-E11718h) kit following manufacturer's instructions ($n = 3$ for each group). To assess tube formation, 100 µL per well of cold Matrigel (Corning, Bedford, MA) was added to a 48-well plate and incubated at 37 °C to afford a gel. At the same time, different aerogel scaffolds of the same mass were immersed in medium (DMEM) containing 10% fetal bovine serum (FBS, Gibco) and 1% penicillin/streptomycin (Hy-Clone), respectively, and incubated at 37 °C for 24 h. Filter through a 0.22 µm filter and carefully collect the sterile supernatant. Thereafter, HUVECs were seeded on the surface of Matrigel at a density of 1×10^4 cells/well, and then incubated with conditioned medium obtained from the scaffolds. Tube formation of HUVECs was observed by using a microscope (DMi 8, Leica, Germany). The total length of imaged tubules, the number of connections, the number of grids, and the total grid area per high-power field (HPF) were quantified by using Image J ($n = 3$ for each group).

Osteogenic Differentiation: The ALP and ARS methods were used to detect the osteogenic differentiation of rBMSCs on the aerogel scaffolds ($n = 3$–4 for each group). The rBMSCs were seeded on aerogel scaffolds with 2×10^5 cells per well and cultured in osteogenic induction medium (The composition contains 10 mmol L^{-1} sodium β-glycerophosphate, 0.05 mmol L^{-1} vitamin C, 100 mmol L^{-1} dexamethasone, and DMEM medium containing 10% FBS). On days 4, 7, and 14, the cells were lysed with Western and IP cell lysate (Beyotime Biotechnology; P00131), and the supernatant was collected from the alkaline phosphatase assay kit (Beyotime Biotechnology; P0321) to determine alkaline phosphate Enzyme (ALP value). The BCA protein analysis kit (Beyotime Biotech; P0012S) was used to normalize the ALP activity to the total protein content of the corresponding scaffold supernatant. The samples were rinsed three times with PBS and fixed with 4% paraformaldehyde. The BCIP/NBT analysis kit (Beyotime Biotechnology; C3206) was used for ALP staining according to the instructions, and the samples were observed by a digital camera and an optical microscope. For ARS test, samples were rinsed three times with PBS, fixed with 4% paraformaldehyde for 30 min, and then immersed in 2% ARS solution (Yuanye Biotechnology, R20796) for 5 min. After washing with PBS several times to remove floating color, stained samples were observed with a digital camera and optical microscope. To further quantify calcium mineralization, the dyed samples were soaked in 10% cetyl pyridinium chloride (Aladdin Chemical; C129534) solution for 1 h at room temperature. The absorbance of samples was recorded at 570 nm by using a microplate reader (Multiskan MK3, Thermo, USA).

To determine the expression of osteogenic related genes, including RUNX2, COL-1, BMP-2, and OPN from PLA/gel and PLA/gel/SiO_2-M aerogel scaffold ($n = 3$ for each group) the total RNA of rBMSCs was collected by using TRIzol reagent (Beyotime, Shanghai, China,15596018) at day 4, 7, and 14 and reverse-transcribed to obtain cDNA by using Reverted First Strand cDNA synthesis kit (Thermo Science, K1622). Quantitative PCR was performed by Novostart9SYBR qPCR SuperMix Plus (NovoProtein, E096-01A, China) in the RT-qPCR system (Applied Biosystems, 7300, USA). The relative gene expressions were calculated using ΔΔCt method by housekeeping dehydrogenase (GAPDH) normalization. The primer sequences used for RT-PCR are shown in Table S1, Supporting Information. Western blot analysis ($n = 3$ for each group) was performed to determine whether the aerogel scaffold was able to promote the expression of the osteogenic-related protein. Supporting Information provides specific operation methods.

In vivo Assessments: The SD rats (age, 6-week) were obtained from Shanghai Jie Sijie Experimental Animal Co. Rats were acclimated for up to 1 week. Animal experiments were reviewed and approved by the ethical committee of Donghua University (No. DHUES-STCSM-2020-01) and were performed in accordance with the Guide for the Care and Use of Laboratory Animals (National Institutes of Health, 8th Edition, revised 2011). Aerogel scaffolds (thickness, 2 mm and diameter, 5 mm) were sterilized. Rats were anesthetized by an intraperitoneal injection of sodium pentobarbital followed by the creation of calvaria defect (diameter, 5 mm). Thereafter, animals received either PLA/gel or PLA/gel/SiO_2 or were left untreated. At 4, 8, and 12 post-operative procedure, the skull was harvested and fixed with 4% paraformaldehyde. Micro-CT (SkyScan 1176, Bruker) was used to analyze the degree of bone repair of different scaffolds, and CT-Analyzer software was used to analyze the ratio of new bone volume to total volume (BV/TV). Then, the bone tissues were decalcified, and the tissues were embedded in paraffin and sectioned. Histological analysis was performed by using H&E staining and Masson's trichrome staining. The stained sections were imaged using an optical microscope (DMi 8, Leica, Germany). Immunofluorescence staining for OCN and OPN was further performed. Angiogenesis around the new bone tissues was observed by immunofluorescence staining of platelet EC adhesion molecule-1 (CD31) and α-SMA. Signal intensities were quantified using Image-Pro Plus software ($n = 4$ for each group). The detailed methods are provided in Supporting Information.

Statistical Analysis: All data were expressed as mean ± standard deviation and analyzed by unpaired Student's *t*-test or one-way analysis of variance and Tukey's post-hoc test. Statistical significance was considered to be $p < 0.05$.

Supporting Information

Supporting Information is available from the Wiley Online Library or from the author.

Acknowledgements

The authors acknowledge financial support from the Fundamental Research Funds for the Central Universities (2232019A3-07), National Nature Science Foundation of China (No. 31771023, 32050410286), Science and Technology Commission of Shanghai Municipality (No.19441902600,

20S31900900, 20DZ2254900), and Sino German Science Foundation Research Exchange Center (M-0263). This project was also supported by Researchers Supporting Project Number (RSP-2021/65), King Saud University, Riyadh, Saudi Arabia, National Advanced Functional Fiber Innovation Center (2021-fx020301), International Cooperation of 2021–2022 China and Poland Science and Technology Personnel Exchange Program (No.17).

Conflict of Interest

The authors declare no conflict of interest.

Data Availability Statement

The data that support the findings of this study are available from the corresponding author upon reasonable request.

Keywords

aerogel scaffolds, angiogenesis, electrospinning, osteogenesis, SiO_2 nanofibers

Received: March 4, 2022
Revised: April 25, 2022
Published online:

[1] a) N. G. Lasanianos, N. K. Kanakaris, P. V. Giannoudis, *Orthopaedics and Trauma* **2010**, *24*, 149; b) M. Rapp, F. Grauel, L. M. Wessel, P. Illing, M. M. Kaiser, *Acta Orthop. Belg.* **2016**, *82*, 723.
[2] W. Jing, A. A. Smith, B. Liu, J. Li, J. A. Helms, *Biomaterials* **2015**, *47*, 29.
[3] T. Hou, Z. Li, F. Luo, Z. Xie, X. Wu, J. Xing, S. Dong, J. Xu, *Biomaterials* **2014**, *35*, 5689.
[4] a) S. V. Dorozhkin, *Biomaterials* **2010**, *31*, 1465; b) P. Ducheyne, Q. Qiu, *Biomaterials* **1999**, *20*, 2287; c) R. Z. LeGeros, *Clin. Orthop. Relat. Res.* **2002**, *395*, 81.
[5] U. Kneser, D. J. Schaefer, E. Polykandriotis, R. E. Horch, *J. Cell. Mol. Med.* **2006**, *10*, 7.
[6] J. Zhang, W. Liu, V. Schnitzler, F. Tancret, J. M. Bouler, *Acta Biomater.* **2014**, *10*, 1035.
[7] M. Stanczyk, B. V. Rietbergen, *J. Biomech.* **2004**, *37*, 1803.
[8] M. Bohner, *Eur. Cells Mater.* **2010**, *20*, 1.
[9] G. Hannink, J. J. C. Arts, *Injury* **2011**, *42*, S22.
[10] A. Mikos, *Polymer* **1994**, 35.
[11] P. X. Ma, R. Zhang, *J. Biomed. Mater. Res.* **1999**, *46*, 60.
[12] W. Chen, Y. Xu, Y. Li, L. Jia, G. Zhou, *Chem. Eng. J.* **2019**, *382*, 122986.
[13] J. Gu, Q. Zhang, M. Geng, W. Wang, J. Yang, A. Khan, H. Du, Z. Sha, X. Zhou, C. He, *Bioact. Mater.* **2021**, *6*, 3254.
[14] G. Duan, S. Jiang, V. Jerome, J. H. Wendorff, A. Fathi, J. Uhm, V. Altstaedt, M. Herling, J. Breu, R. Freitag, *Adv. Funct. Mater.* **2015**, *25*, 2850.
[15] W. Chen, S. Chen, Y. Morsi, H. El-Hamshary, M. El-Newhy, C. Fan, X. Mo, *ACS Appl. Mater. Interfaces* **2016**, *8*, 24415.
[16] M. Mader, V. Jerome, R. Freitag, S. Agarwal, A. Greiner, *Biomacromolecules* **2018**, 1663.
[17] X. He, N. Kawazoe, G. Chen, *Biomed Res. Int.* **2014**, *2014*, 106082.
[18] J. I. Lim, H. K. Park, *J. Porous Mater.* **2012**, *19*, 383.
[19] L. Wang, Y. Qiu, H. Lv, Y. Si, L. Liu, Q. Zhang, J. Cao, J. Yu, X. Li, B. Ding, *Adv. Funct. Mater.* **2019**, *29*, 1901407.
[20] W. Zhai, H. Lu, C. Wu, L. Chen, C. Jiang, *Acta Biomater.* **2013**, *9*, 8004.
[21] a) H. Li, K. Xue, N. Kong, K. Liu, J. Chang, *Biomaterials* **2014**, *35*, 3803; b) S. Choi, G. Seung, S. Lee, S. Im, H. Seong, *J. Mater. Sci. Lett.* **2003**, *22*, 891.
[22] F. J. O'Brien, *Mater. Today* **2011**, *14*, 88.
[23] K. Ye, D. Liu, H. Kuang, J. Cai, W. Chen, B. Sun, L. Xia, B. Fang, Y. Morsi, X. Mo, *J. Colloid Interface Sci.* **2019**, *534*, 625.
[24] L. Wang, A. Lu, Z. Xiao, J. Ma, Y. Li, *Appl. Surf. Sci.* **2009**, *255*, 7542.
[25] I. V. Yannas, A. V. Tobolsky, *Nature* **1967**, *215*, 509.
[26] a) C. L. Sadowsky, J. W. Mcdonald, *Developmental Disabilities Research Reviews* **2010**, *15*, 112; b) W. A. El-Kheir, H. Gabr, M. R. Awad, O. Ghannam, Y. Barakat, M. Haithem, A. Farghali, Zeinab, E. Maadawi, I. Ewes, *Cell Transplant.* **2014**, *23*, 729.
[27] L. N. Woodard, K. T. Kmetz, A. A. Roth, V. M. Page, M. A. Grunlan, *Biomacromolecules* **2017**, *18*, 4075.
[28] a) E. Alsberg, *Crit. Rev. Oral Biol. Med.* **2001**, *12*, 64; b) B. L. Eppley, *Journal of Craniofacial Surgery* **2003**, *14*, 144; c) S. H. Lee, C. J. Yoo, U. Lee, C. W. Park, S. G. Lee, W. K. Kim, *Korean Journal of Neurotrauma* **2014**, *10*, 10.
[29] L. Weng, S. K. Boda, M. J. Teusink, F. D. Shuler, X. Li, J. Xie, *ACS Appl. Mater. Interfaces* **2017**, *9*, 24484.
[30] L. Wang, Y. Qiu, Y. Guo, Y. Si, B. Ding, *Nano Lett.* **2019**.
[31] a) *J. Biomed. Mater. Res., Part A* **2009**, 90a; b) J. Ratanavaraporn, R. Rangkupan, H. Jeeratawatchai, S. Kanokpanont, S. Damrongsakkul, *Int. J. Biol. Macromol.* **2010**, *47*, 431.
[32] A. Bigi, G. Cojazzi, S. Panzavolta, N. Roveri, K. Rubini, *Biomaterials* **2002**, *23*, 4827.
[33] S. Xu, K. Lin, Z. Wang, C. Jiang, W. Lin, J. Lu, C. Ning, *Biomaterials* **2008**, *29*, 2588.
[34] L. H. Cao, B. Q. Yu, G. S. Wu, J. C. Su, *J. Inorg. Mater.* **2011**, *26*, 591.
[35] a) L. L. Hench, J. M. Polak, *Science* **2002**, *295*, 1014; b) C. Wu, J. Chang, W. Zhai, S. Ni, J. Wang, *J. Biomed. Mater. Res., Part B* **2006**.
[36] J. B. Vines, D.-J. Lim, J. Lim, J. M. Anderson, H.-W. Jun, *Acta Biomater.* **2012**, *8*, 4053.
[37] J. Glowacki, *Clin. Orthop. Relat. Res.* **1998**, *355*, 82.
[38] A. G. Robling, A. B. Castillo, C. H. Turner, *Annu. Rev. Biomed. Eng.* **2006**, *8*, 455.
[39] J. B. Lian, G. S. Stein, A. Javed, A. Wijnen, J. L. Stein, M. Montecino, M. Q. Hassan, T. Gaur, C. J. Lengner, D. W. Young, *Rev. Endocr. Metab. Disord.* **2006**, *7*, 1.
[40] J. Xue, M. He, H. Liu, Y. Niu, A. Crawford, P. D. Coates, D. Chen, R. Shi, L. Zhang, *Biomaterials* **2014**, *35*, 9395.

